

RADIATION DAMAGE IN SILICON DIODES



by

Dante Rafael Gordon

B.S. in Physics, University of California Los Angeles, 2013

A THESIS SUBMITTED IN PARTIAL FULFILLMENT OF THE REQUIREMENTS FOR

THE DEGREE OF MASTER OF SCIENCE

IN THE DEPARTMENT OF PHYSICS AT BROWN UNIVERSITY

Providence, Rhode Island

May 2017

© Copyright 2017 by Dante Rafael Gordon

This thesis by Dante Rafael Gordon is accepted in its present form by
the Department of Physics as satisfying the
thesis requirement for the degree of
Master of Science

Date.....
Ulrich Heintz, Advisor

Approved by the Graduate Council

Date.....
Andrew G. Campbell,
Dean of the Graduate School

Preface and Acknowledgments

Many people have contributed in one way or another to the completion of this thesis. It is impossible to thank everyone individually; however, I would like to mention a few of them.

I would like to thank my advisor, Professor Ulrich Heintz, for his guidance and encouragement throughout this process. I'm especially grateful for the research opportunities he provided me. I would also like to thank Robert Harrington for his constant support, advice, and generous reading of the drafts of this work. Finally, thank you to Sinan Sagir for his thoughtfulness and willingness to help in any way, especially by answering my myriad of questions with patience.

From the Brown Silicon Lab, I would like to thank all of my colleagues, especially, Soumya Ghosh, who was integral in helping me collect the necessary data, Mary Hadley, for her friendship and encouragement, and Juhi Rahjans who was consistently able to free me of stress.

As always, I would like to thank my family who sent their support from the opposite coast. Especially my mother, who will forever be my biggest fan. Finally, I would like to thank Alys for her love and unwavering encouragement.

Contents

Preface and Acknowledgments	iv
Contents	v
List of Figures	vii
1 Introduction	1
1.1 The Silicon Tracker	3
1.2 Silicon Diodes	4
1.2.1 Basic Operation	4
1.2.2 Biasing	5
1.2.3 Diodes as Ionization Chambers	6
1.3 The Band Gap	7
2 Radiation Damage	8
2.1 Bulk Damage	8
2.1.1 NIEL Scaling Hypothesis	8
2.2 Parametrization	9
2.2.1 Leakage Current	10
2.2.2 Effective Doping Concentration	10
2.2.3 Type Inversion	12
2.3 Annealing	13
2.3.1 Leakage Current	13
2.3.2 Effective Doping Concentration	14
2.3.2.1 Stable Damage	15
2.3.2.2 Short-Term Annealing	15

2.3.2.3	Reverse Annealing	16
3	Experimental Setup	17
3.1	Test Structures	17
3.2	Electrical Characterization (CVIV)	17
3.2.1	Current-Voltage Measurement (IV)	19
3.2.2	Capacitance-Voltage Measurement (CV)	19
3.2.3	Variable Control	20
3.2.3.1	Temperature Control	20
3.2.3.2	Dew Point Control	20
3.2.3.3	Humidity Control	20
4	Analysis	21
4.1	Parameter Extraction	22
4.2	Results	23
4.2.1	Current Related Damage Rate	24
4.2.2	Effective Doping Concentration	24
4.2.3	Error Propagation	24
5	Conclusions	25
5.1	Current Related Damage Rate	25
5.2	Effective Doping Concentration	25
5.3	The Future	26

List of Figures

1.0.1 The LHC outline.	1
1.0.2 Integrated particle fluence in 1 MeV n_{eq} per cm^2 , for the CMS Phase-2 tracker. The estimates shown correspond to a total integrated luminosity of 3000 fb^{-1} of pp collisions at $\sqrt{s} = 14 \text{ TeV}$	2
1.1.1 An overview of the tracker components.	3
1.1.2 The pixel detector.	3
1.2.1 An unbiased diode where the depletion zone has formed.	4
1.2.2 A diode under bias.	5
1.2.3 Current versus voltage for different biases.	6
1.3.1 An energy diagram for different materials.	7
2.1.1 The displacement damage cross-section, normalized to 95 MeV·mb, for different par- ticles. Due to the normalization, the ordinate represents the damage equivalent to 1 MeV neutrons.	9
2.2.1 Dependence of $ N_{\text{eff}} $ (right axis) on 1 MeV neutron equivalent fluence for an n-type diode.	11
2.3.1 The change in α with annealing time at different annealing temperatures.	13
2.3.2 ΔN_{eff} versus annealing time for 60°C annealing temperature.	14
3.1.1 Large diode test structure.	18
3.2.1 A picture of the electrical characterization setup in the Brown Silicon Lab.	18
3.2.2 A drawing of the electrical characterization setup.	19
4.0.1 A typical CVIV plot of voltage versus capacitance. This particular plot is of the diode MCZ200N.	21
4.1.1 A typical plot of $1/C^2$ versus voltage. This particular plot is of the diode MCZ200N.	22

4.1.2 A plot of the extraction procedure for diode MCZ200N.	23
5.3.1 The change in the current related damage rate at 0°C.	27
5.3.2 The change in the current related damage rate at -20°C.	28
5.3.3 The change in the current related damage rate at -20°C.	29
5.3.4 The change in the effective doping concentration at 0°C.	30
5.3.5 The change in the effective doping concentration at -20°C.	31
5.3.6 The change in the effective doping concentration at -20°C.	32

Chapter 1

Introduction

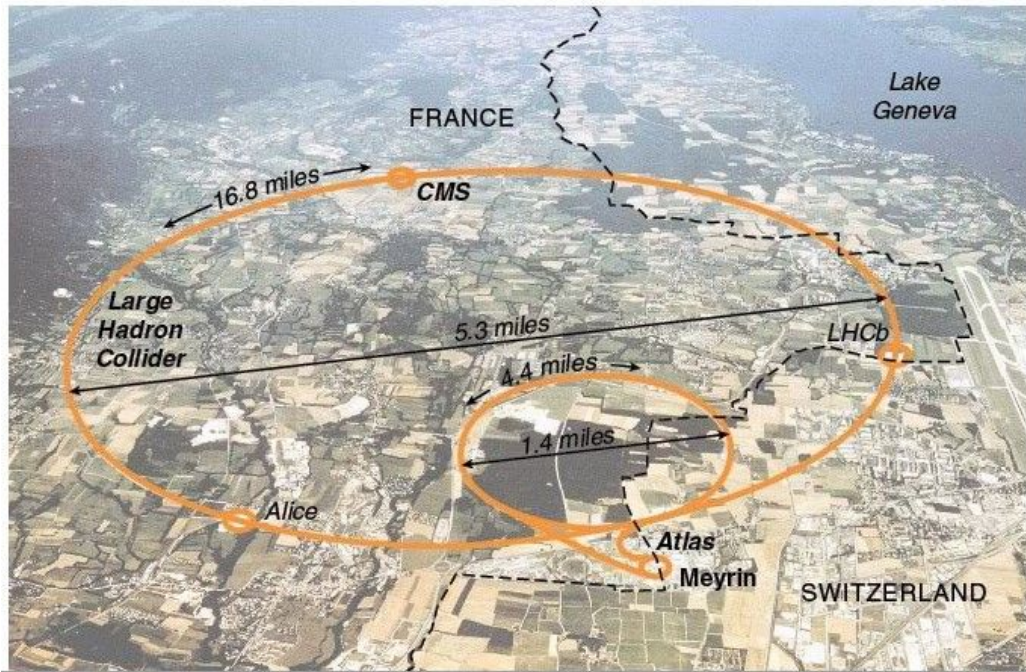


Figure 1.0.1: The LHC outline.

The Compact Muon Solenoid Experiment (CMS) seeks to broaden our understanding of the fundamental particles that make up the universe. CMS is located at the Large Hadron Collider (LHC), the world's largest and most powerful particle accelerator. The LHC consists of a large ring of superconducting magnets, which is 5.3 miles in diameter. The magnets accelerate protons to speeds close to the speed of light, with an energy of 6.5 TeV per proton. CMS surrounds the beam line and uses multiple layers of detectors to track the particles that result from proton collisions in the collider.

The main goals of the CMS experiment are to study the properties of the Higgs boson, study the physics of particles at the TeV scale, test hypotheses such as supersymmetry, and look for completely new phenomena. The detector itself is made of many layers, each layer being designed to detect the different particles resulting from the collisions in the beam line. The layers consist of a silicon tracker, multiple calorimeters, and muon detectors. It is the phase-2 upgrade of the silicon tracker which is the focus of this work.

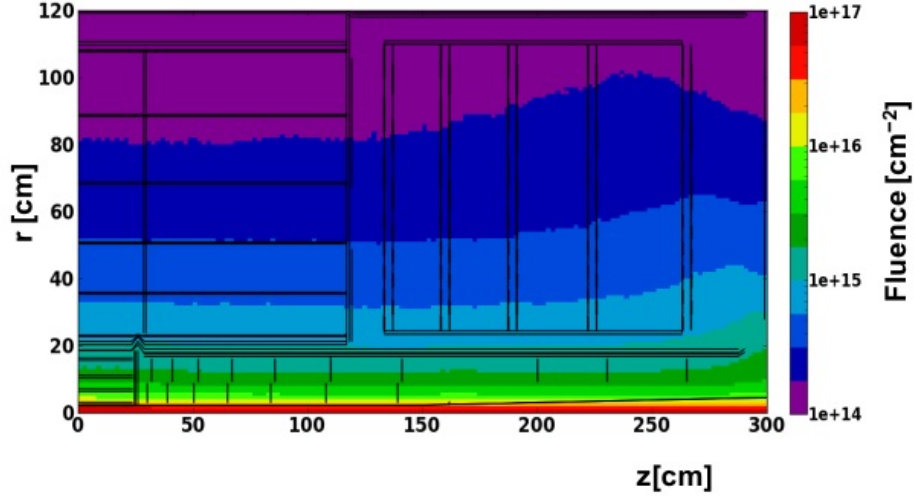


Figure 1.0.2: Integrated particle fluence in $1 \text{ MeV } n_{\text{eq}}$ per cm^2 , for the CMS Phase-2 tracker. The estimates shown correspond to a total integrated luminosity of 3000 fb^{-1} of pp collisions at $\sqrt{s} = 14 \text{ TeV}$.

In the second phase of the LHC program the High Luminosity-Large Hadron Collider (HL-LHC) will provide CMS an additional integrated luminosity of approximately 2500 fb^{-1} over 10 years of operation [2]. This equates to nominal luminosities of approximately 5.0×10^{34} per $\text{s} \cdot \text{cm}^2$. Since the tracker is right next to the beam line, it experiences the largest particle fluences. As shown in Figure 1.0.2, the pixel detector could receive upwards of $1.0 \times 10^{16} \text{ 1 MeV } n_{\text{eq}} \cdot \text{cm}^{-2}$ and the strip detectors upwards of $1.0 \times 10^{15} \text{ 1 MeV } n_{\text{eq}} \cdot \text{cm}^{-2}$. This much radiation, as one can imagine, causes damage to the tracker; so much so, in fact, that some have postulated that the tracker will not last the full time period of the experiment [1]. For this reason, the development of radiation hard materials for the tracker is of the utmost importance.

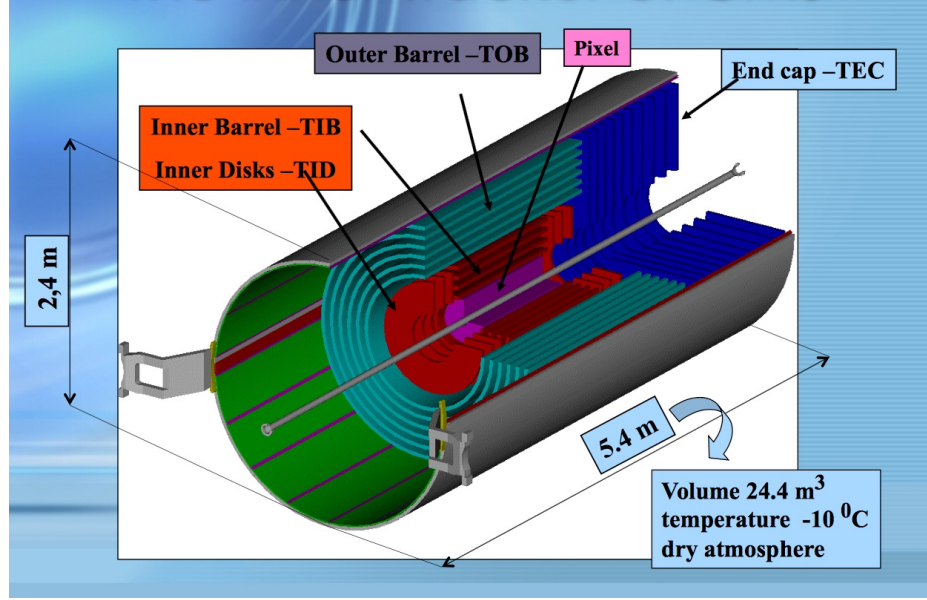
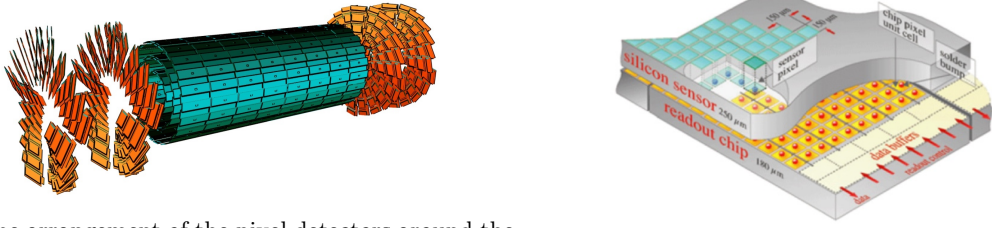


Figure 1.1.1: An overview of the tracker components.



(a) The arrangement of the pixel detectors around the beam line.

(b) The pixel detector geometry.

Figure 1.1.2: The pixel detector.

1.1 The Silicon Tracker

The first detector encountered by particles is the silicon tracker. The tracker is used to reconstruct the paths of particles that have traveled through it with high accuracy. The tracker is made up of two separate types of sensors, the pixel detectors (seen in purple in Figure 1.1.1) and the strip detectors (seen in teal, red, and blue in Figure 1.1.1). Both types of sensors act as ionization chambers to reconstruct particle paths.

Shown in Figure 1.1.2b, each pixel sensor is made of approximately 65 million pixels and each pixel is a separate detector (with its own dedicated electronics). Because each pixel is approximately a square, 100 microns by 150 microns, the pixel detector is able to yield two-dimensional position information on a particle's path. The pixel detector is closest to the beam line, starting at a radius of ~ 4 cm and ending at a radius of ~ 10 cm, and arranged into the barrel and the “endcaps”, represented

in Figure 1.1.2a by the teal structure and the orange structures, respectively.

The strip detectors surround the pixel detector barrel and endcaps in multiple cylindrical layers, ten in all, out to a radius of 130 cm. Each strip detector module is made of strip channels, which are able to give one-dimensional resolution of particle tracks because the module is much longer than the distance between successive strips. Thus, in one dimension (the longer one) the resolution is much lower than the other dimension.

1.2 Silicon Diodes

1.2.1 Basic Operation

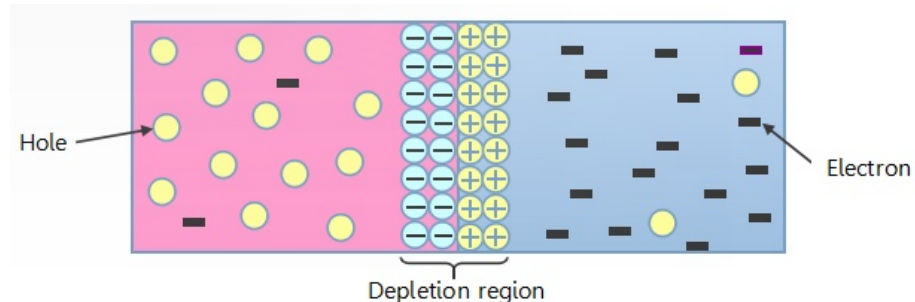
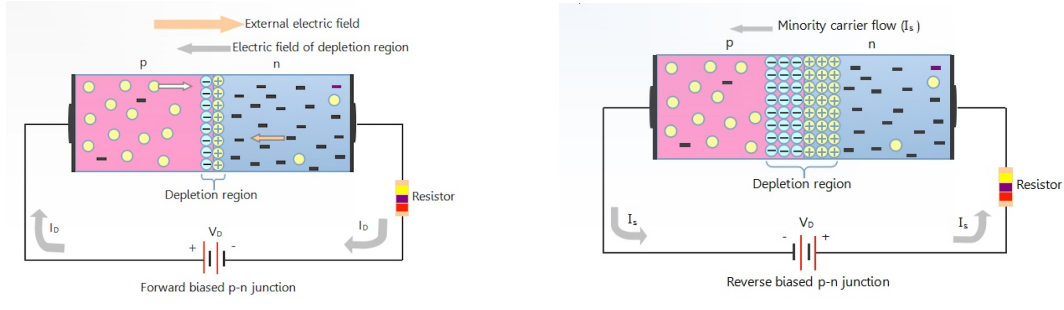


Figure 1.2.1: An unbiased diode where the depletion zone has formed.

A diode is formed when a p-type material, where holes are the majority charge carriers, and a n-type material, where electrons are the majority charge carriers, are put in contact. At the location of contact, known as the “p-n junction”, a region free of charge carriers is formed. This “depletion zone”, or “depletion region”, can be understood by examining what happens to the charge carriers on each side of the junction. When the two material types are brought together, shown in Figure 1.2.1, electrons from the n-type material diffuse into the p-type material causing negatively charged ions to be created near the junction; the same can be said of holes from the p-type material. At some point, there are so many of the negatively charged ions near the junction that the rest of the electrons are repelled from entering the p-type material; the same can be said of the positively charged ions inside the n-type region. Thus, the depletion region is established.

The build-up of negatively charged ions in the p-type, and positively charged ions in the n-type, material creates an electric field across the junction, corresponding to a potential called the “built-in potential”, or “built-in voltage”. When an outside voltage is applied to the diode, called “biasing”, the width of the depletion zone changes depending on the “direction” of the bias. The width of the



(a) A diode being forward biased.

(b) A diode being reverse biased.

Figure 1.2.2: A diode under bias.

depletion region will become very important later on.

1.2.2 Biasing

Biasing refers to the application of an outside voltage to a diode. There are two “directions” a diode can be biased, “forward” and “reverse”. A forward bias is a connection in which the positive terminal of the battery is connected to the p-type material and the negative terminal to the n-type material (see Figure 1.2.2a). Since the electric field set up by the battery is in the opposite direction to that of the electric field initially setup in the depletion zone, the total electric field across the depletion zone is reduced allowing charge carriers to once again cross the junction. As electrons, which are attracted to the positive terminal of the battery, travel into the p-type material they fill some of the vacant orbitals in the positive ions in the depletion zone. The same can be said for the holes traveling toward the n-type material. Because of this the width of the depletion zone **decreases** under forward bias.

Figure 1.2.3a shows how the current varies with voltage applied to a forward biased diode. As the voltage is increased there is no increase in current until the built-in voltage is reached. At this point, the electric field setup by the battery overcomes the electric field of the depletion zone and charge is “allowed” to flow across the junction.

A reverse bias is connection in which the positive terminal of the battery is connected to the n-type material and the negative terminal of the battery is connected to the p-type material (see Figure 1.2.2b). Note that now the electric field setup by the battery is in the same direction as that of the original electric field across the depletion zone, making it more difficult for majority charge carriers to cross the depletion zone (minority charge carriers can still flow). Since the positive terminal of the battery is connected to the n-type material, electrons will start to travel away from the depletion zone. As they move toward the positive terminal they will leave ion cores behind; the

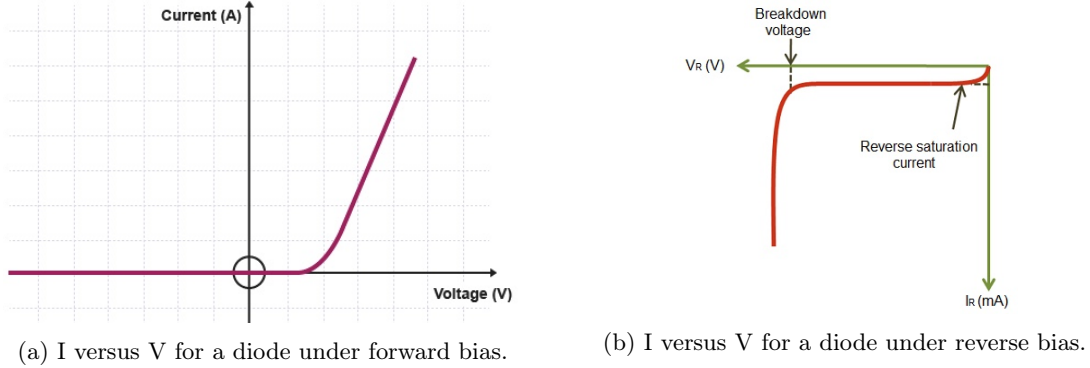


Figure 1.2.3: Current versus voltage for different biases.

same can be said for holes in the p-type material. The result is that the width of the depletion zone **increases** under reverse bias. The voltage necessary to widen the depletion zone to the geometric width of the diode itself is called the “depletion voltage”. This depletion voltage is key to forming an ionization chamber.

Figure 1.2.3b shows how the current varies with voltage applied to a reverse biased diode. Recall that there can still be a minority carrier flow across the junction in a reverse bias setup. This minority carrier flow results in a very small current, on the order of nanoamps for silicon, called the “reverse saturation current,” or “leakage current”. This leakage current reaches a maximum very quickly and does not vary much with increasing reverse bias voltage. However, when the voltage reaches a certain limit, called the “breakdown voltage,” the current increases drastically.

1.2.3 Diodes as Ionization Chambers

Ionization chambers are powerful tools in particle physics because they track the paths of particles that have traveled through them. Classically, an ionization chamber is filled with a material or gas and oppositely charged plates are placed at either end, which generates an electric field in the chamber. As an incident particle travels through the chamber, it ionizes the atoms in its path creating electron-hole pairs, which are then guided to the plates by the electric field. When the charge reaches the plates it creates a current, which is then measured.

In order for a diode to function as an ionization chamber, the number of free charge carriers must be minimized. This means that the width of the depletion region must equal the geometric width of the diode. When this occurs, or when the diode has been “fully depleted”, most of the charge carriers present are those created by the incident particles.

1.3 The Band Gap

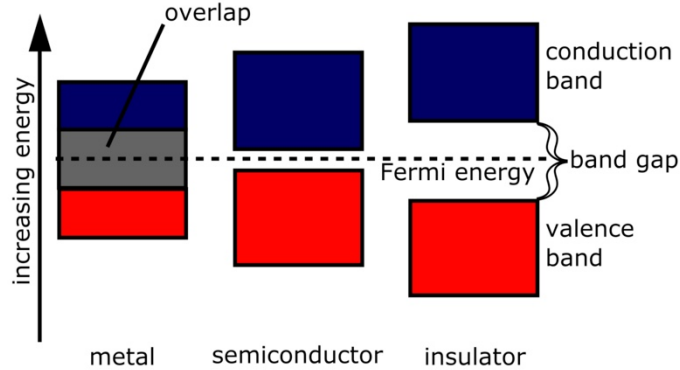


Figure 1.3.1: An energy diagram for different materials.

The behavior of a semiconductor, like silicon, can be explained using an energy level diagram like the one shown in Figure 1.3.1. The energy levels present in the “valence band” are those where the electron is bound to an atom, while the energy levels present in the “conduction band” are those where the electrons are free to move through the material and conduct electricity. The “band gap” is the difference in energy between the valence band and the conduction band. It is the amount of energy that an electron would need to leave an atom. Radiation damage creates new energy levels within the band gap, which changes the behavior of the material.

Chapter 2

Radiation Damage

Radiation damage can be organized into two types: bulk damage and surface damage. Since bulk damage is the limiting factor in high energy particle (HEP) experiments, only bulk damage will be discussed. For a more detailed discussion of surface damage see [1].

2.1 Bulk Damage

The first target atom encountered by an incident particle is called the “primary knock-on atom” (PKA). After the collision of the incident particle and the PKA, the PKA is displaced from its position in the silicon leaving behind a vacancy in the lattice. If the PKA has enough energy, the minimum being 25 eV for silicon [1], it can displace other silicon atoms causing a cascade. If it does not have enough energy it can come to rest in a random location creating an interstitial defect. The vacancy left by the PKA and the interstitial defect it forms is called a “Frenkel pair”. The bulk damage accounts for most of the changes in the detector properties. The exact changes in particular parameters and the mechanisms for these changes will be discussed in Section 2.2.

2.1.1 NIEL Scaling Hypothesis

The Non-Ionizing Energy Loss (NIEL) hypothesis assumes that the bulk damage is proportional to the kinetic energy imparted to the displaced silicon atoms. It also assumes that this relationship exists no matter the spatial distribution of the PKA cascade and the annealing steps taken after the initial damage occurs. Using these assumptions, the “displacement damage cross-section,” $D(E)$, can be computed. The details of the derivation of the displacement damage cross-section are beyond the scope of this thesis, but the function $D(E)$ for different particles is shown in Figure 2.1.1. The

Displacement damage functions

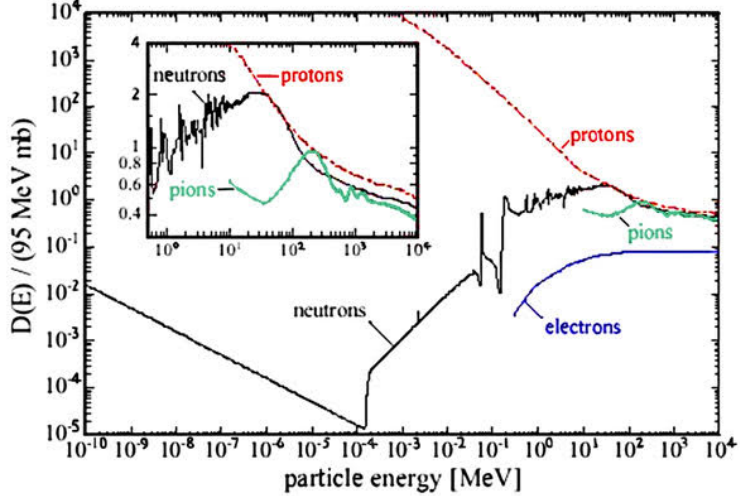


Figure 2.1.1: The displacement damage cross-section, normalized to 95 MeV·mb, for different particles. Due to the normalization, the ordinate represents the damage equivalent to 1 MeV neutrons.

displacement damage cross-section yields the relative efficiency with which an incident particle with energy E can create PKAs. Using this function, an equation relating the experimental fluence and the equivalent neutron fluence can be found.

$$\Phi_{\text{eq}} = \kappa \Phi_{\text{exp.}} \quad (2.1.1)$$

The “hardness factor,” κ , is defined to be one for 1 MeV neutrons. Thus, using Equation 2.1.1, one can calculate the fluence of 1 MeV neutrons necessary to create the same damage as any experimental fluence used. This means that two different people can use two different types of particles at two different energies to irradiate their silicon sensors and still be able to compare their data concerning the changes to sensor properties.

2.2 Parametrization

In order to determine how to develop radiation hard silicon detectors for the tracker, characterization experiments were performed on silicon diodes. The radiation damage effects leakage current and effective doping concentration the most. Radiation damage also effects charge collection efficiency (CCE), which accounts for the ability of the detector to collect the e-h pairs created by the

incident particle. However, the change in CCE is negligible compared to the other two parameters and could not be measured in the time allotted for this work [1].

The leakage current, which accounts for noise in the detector, increases proportionally to fluence. The depletion voltage, which, as mentioned earlier, is necessary for the detector to function as an ionization chamber and is directly connected with the effective doping concentration, also increases with increasing fluence.

2.2.1 Leakage Current

In general, the leakage current is any current flowing through a device when, ideally, no current should flow, like when the device is turned off. As mentioned in Section 1.2.2, the leakage current here refers to reverse leakage current; present before the breakdown of a reverse biased diode. In the non-irradiated case, the leakage current is caused by majority charge carriers, electrons in the n-type and holes from the p-type, crossing the junction (“diffusion current”) and from the generation of charge carriers in the depletion zone (“generation current”). In the irradiated case, new energy levels form near the middle of the band gap generating electron-hole pairs. For a more complete discussion of this phenomenon see [1] and [4]. After irradiation, defects in the depletion zone cause increases in the generation current, which increases the overall leakage current. It has been experimentally shown by [1] that the leakage current increases with fluence according to,

$$\frac{\Delta I}{V} = \alpha \Phi_{\text{eq}} \quad (2.2.1)$$

where ΔI is the difference between the leakage current before and after irradiation, V is the volume of the fully depleted diode, and α is called the “current related damage rate”. The current related damage rate is independent of the type of silicon material, particle used during irradiation, and particle energy [1].

2.2.2 Effective Doping Concentration

The effective doping concentration, N_{eff} , is the difference between the concentration of ionized donors and acceptors, or the space charge, in the volume of the depletion zone. It can be derived using Poisson’s equation and the full-depletion approximation, which states that the depletion zone is fully depleted and has well defined edges. This process yields the width of the depletion zone as a function of the voltage applied to the diode,

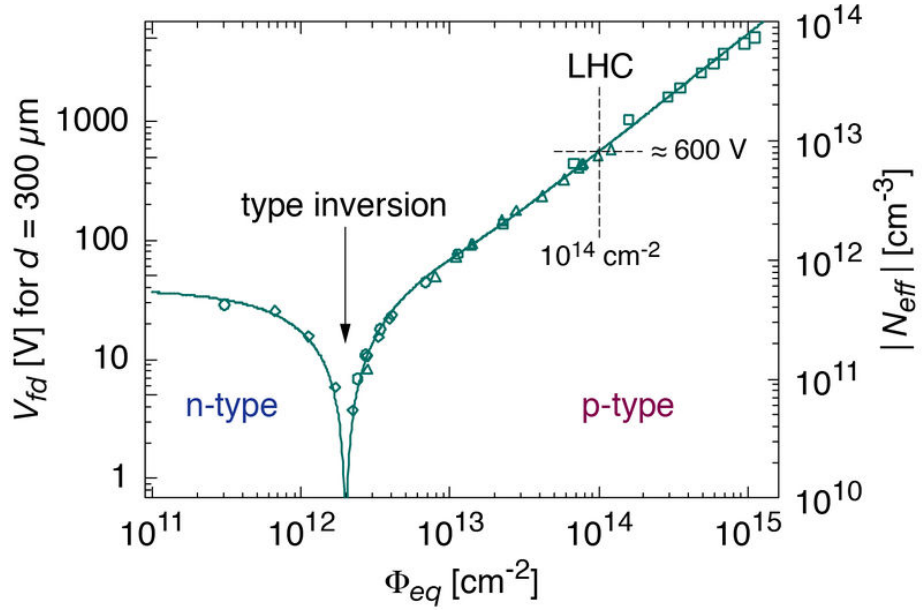


Figure 2.2.1: Dependence of $|N_{\text{eff}}|$ (right axis) on 1 MeV neutron equivalent fluence for an n-type diode.

$$w(V) = \sqrt{\frac{2\epsilon_s\epsilon_0}{q_0|N_{\text{eff}}|}(V + V_{\text{bi}})} \quad (2.2.2)$$

where ϵ_s is the relative permittivity of silicon, ϵ_0 is the permittivity of free space, q_0 is the magnitude of the charge of the carriers (the electron charge), and V_{bi} is the built-in voltage. When the diode is fully depleted $V = V_{\text{dep}}$ and,

$$V_{\text{dep}} + V_{\text{bi}} = \frac{q_0}{2\epsilon_0\epsilon_s}|N_{\text{eff}}|W^2 \quad (2.2.3)$$

where W is the width of the fully depleted diode. The built-in voltage is, in almost all cases, a full order of magnitude smaller than the depletion voltage and thus, it is neglected. Taking this into account, the effective doping concentration is related to the depletion voltage by,

$$|N_{\text{eff}}| = \frac{2\epsilon_0\epsilon_s}{q_0W^2}|V_{\text{dep}}|. \quad (2.2.4)$$

Note that in both Equation 2.2.3 and Equation 2.2.4 the depletion voltage is being related to the absolute value of the effective doping concentration.

We can also use Equation 2.2.2 to relate the voltage to the capacitance of the diode, which will become important later. We know that,

$$C = \frac{dQ}{dV},$$

so we can also write,

$$C = \frac{dQ}{dw} \frac{dw}{dV}.$$

Now we need the space charge as a function of the width of the depletion zone, $Q(w)$. Given the definition of N_{eff} (see above), we can say that,

$$Q = q_0 N_{\text{eff}} A w(V),$$

where A is the active area of the diode. Taking derivatives and doing some algebra yields,

$$C(V) = \frac{\epsilon_s \epsilon_0 A}{w(V)} = A \sqrt{\frac{\epsilon_s \epsilon_0 q_0 |N_{\text{eff}}|}{2(V + V_{\text{bi}})}}. \quad (2.2.5)$$

Equation 2.2.5 holds as long as $V \leq V_{\text{dep}}$, which implies that $w(V) \leq W$. When $V = V_{\text{dep}}$, $w = W$ and

$$C(V_{\text{dep}}) = C_{\text{geo}} = \frac{\epsilon_s \epsilon_0 A}{W}, \quad (2.2.6)$$

called the “geometric capacitance” of the diode because this is the equation we would get if the diode were treated as a regular capacitor with a dielectric.

2.2.3 Type Inversion

As shown in Figure 2.2.1, $|N_{\text{eff}}|$ decreases with increasing fluence until a particular fluence where the sensor undergoes something called “type inversion”. Due to details that are beyond the scope of this thesis (new energy levels in the band gap), radiation is more likely to create “acceptor like” defects than “donor like” defects. As a result of this, the silicon becomes more and more p-doped as it is exposed to more and more radiation. This does nothing to a p-type diode, as it is already p-doped. Thus, in the p-type diodes, $|N_{\text{eff}}|$ continues to increase with increasing fluence. However, for an n-type diode, the increasing positive space charge created by the acceptor like defects causes

a type inversion where the n-type diode begins to behave like a p-type diode. Thus, after the type inversion occurs, $|N_{\text{eff}}|$ begins to increase with increasing fluence, just as with a p-type diode.

2.3 Annealing

Annealing refers to heating a diode at a certain temperature for a certain length of time in an oven. In some ways, annealing can actually improve the function of the silicon by “healing” defects. By heating the material, some of the atoms that have been displaced become mobile again and fill vacancies left by other displaced atoms. The effects of annealing on radiation damaged silicon have been well documented and will be briefly reviewed in this section.

2.3.1 Leakage Current

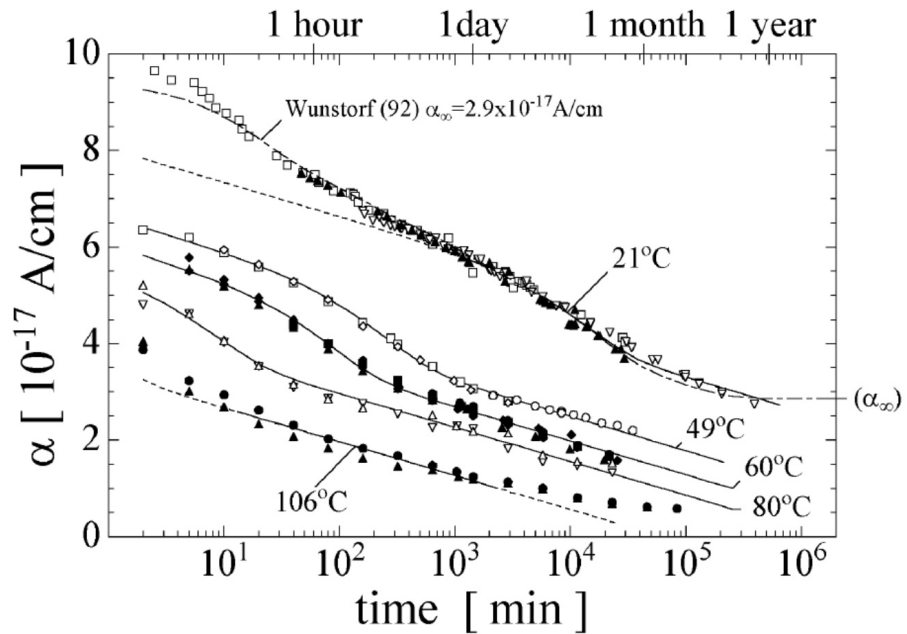


Figure 2.3.1: The change in α with annealing time at different annealing temperatures.

The change in leakage current with annealing time is investigated by monitoring the current related damage rate. The current related damage rate is highly temperature dependent according to the equation,

$$\alpha(t) = \alpha_i e^{-\tau t} + \alpha_0 - \beta \ln \left(\frac{t}{t_0} \right) \quad (2.3.1)$$

where

$$\tau = ke^{-\gamma/k_B T_{\text{ann}}} \quad (2.3.2)$$

and α_i , α_0 , β , k , and γ are all parameters, which are detailed in [1]. Note that T_{ann} in Equation 2.3.2 is the annealing temperature. Shown in Figure 2.3.1, α does indeed decrease with annealing.

2.3.2 Effective Doping Concentration

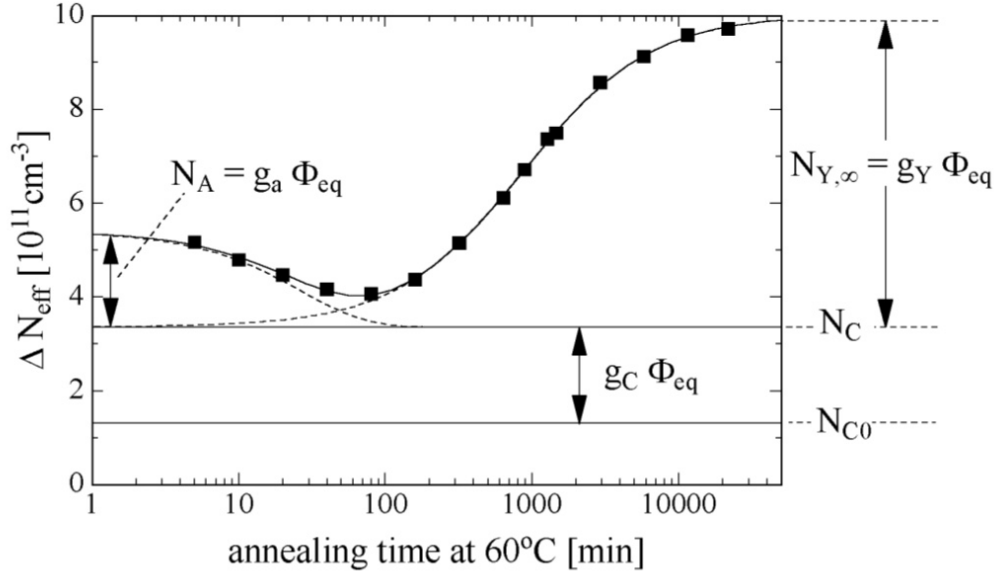


Figure 2.3.2: ΔN_{eff} versus annealing time for 60°C annealing temperature.

The overall change in effective doping concentration can be described using the Hamburg Model. The Hamburg Model takes into account both the change due to annealing and the change due to irradiation. Defining,

$$\Delta N_{\text{eff}}[\Phi_{\text{eq}}, t(T_{\text{ann}})] = N_{\text{eff},0} - N_{\text{eff}}[\Phi_{\text{eq}}, t(T_{\text{ann}})] \quad (2.3.3)$$

where $N_{\text{eff},0}$ is the effective doping concentration before irradiation. Note that the time, t , is also a function of annealing temperature. This total change in N_{eff} can be described by three terms,

$$\Delta N_{\text{eff}}[\Phi_{\text{eq}}, t(T_{\text{ann}})] = N_A[\Phi_{\text{eq}}, t(T_{\text{ann}})] + N_C(\Phi_{\text{eq}}) + N_Y[\Phi_{\text{eq}}, t(T_{\text{ann}})] \quad (2.3.4)$$

where N_A is the “short-term annealing” component, N_C is the “stable damage” component, and N_Y is the “reverse annealing” component.

2.3.2.1 Stable Damage

The stable damage component is expressed as,

$$N_C(\Phi_{\text{eq}}) = N_{C,0} (1 - e^{-c\Phi_{\text{eq}}}) + g_c \Phi_{\text{eq}} \quad (2.3.5)$$

where $N_{C,0}$ is the initial concentration of removable donors, c is the removal constant, and g_c is the acceptor introduction rate. The first term describes the donor removal as the material is irradiated; recall that the material becomes increasingly p-doped. The product of the removal constant and the initial concentration of removable donors is a constant and is called the “initial donor removal rate,”

$$N_{C,0} \cdot c = (7.5 \pm 0.6) \times 10^{-2} \text{ cm}^{-1}.$$

The second term in Equation 2.3.5 describes the acceptor formation where the typical value for the acceptor formation rate, g_c , is $1.5 \times 10^{-2} \text{ cm}^{-1}$ [5].

2.3.2.2 Short-Term Annealing

The short-term annealing can be represented as a sum of exponentials,

$$N_A = \Phi_{\text{eq}} \sum_i g_{a,i} e^{-t/\tau_{a,i}},$$

but annealing time constants, $\tau_{a,i}$, in minutes and hours are too short to be relevant in an actual experiment. Thus, N_A can be approximated by the exponential,

$$N_A \approx \Phi_{\text{eq}} g_a e^{-t/\tau_a} \quad (2.3.6)$$

where $g_a = (1.81 \pm 0.14) \times 10^{-2} \text{ cm}^{-1}$ and τ_a is,

$$\frac{1}{\tau_a} = k_{a,0} e^{-E_a/k_B T_{\text{ann}}} \quad (2.3.7)$$

The constant $k_{a,0}$ depends on the type of silicon and E_a is the activation energy.

2.3.2.3 Reverse Annealing

The long-term annealing, or reverse annealing can be described by

$$N_Y = \Phi_{\text{eq}} g_y \left(1 - \frac{1}{1 + t/\tau_y} \right), \quad (2.3.8)$$

where $g_y = (5.16 \pm 0.09) \times 10^{-2} \text{ cm}^{-1}$ and τ_y is,

$$\frac{1}{\tau_y} = k_{y,0} e^{-E_y/k_B T_{\text{ann}}}. \quad (2.3.9)$$

The constant $k_{y,0}$ depends on the type of silicon and E_y is the activation energy. There is much debate over this parametrization. For a full discussion, see [1].

Chapter 3

Experimental Setup

3.1 Test Structures

The test structures being studied consisted of diodes produced using Float Zone (FZ), Magnetic Czochalski (MCz), and Thinned FZ (FTH) manufacturing techniques. For a more detailed description of the process of manufacture for each type, see [1]. For this work, only certain diodes were able to be tested; for brevity, they have been given names that declare the manufacturing process, the type, and the thickness. The naming scheme is as follows: (Manufacture Process, Thickness (μm), and Type of Diode). For example: FZ200P is a float zone, p-type diode, with a thickness of 200 μm . The diodes can also be categorized by large versus small. The “large diodes”, shown in Figure 3.1.1, consisted of a bias ring, shown in red in Figure 3.1.1b, and a guard ring (used to ground the diode), shown in blue in Figure 3.1.1b. They also, obviously, had a larger active area, 25 mm^2 , compared with the “small” diodes, which had an active area of 6.25 mm^2 . The small diodes consisted only of a bias ring. All test structures were irradiated with 800 MeV protons at fluences up to $1.5 \times 10^{15} n_{\text{eq}} \text{ cm}^{-2}$.

3.2 Electrical Characterization (CVIV)

Electrical Characterization is done using the setup shown in Figure 3.2.1. Each diode is held onto a temperature controlled “chuck,” which is a solid piece of aluminum, by vacuum pumping. An acrylic box is placed over the chuck and dry air or nitrogen is pumped into it to create a more controlled environment. During the measurement the dew point is constantly tracked to ensure no condensation forms on the diodes. The diodes are biased from the rear electrode by applying a

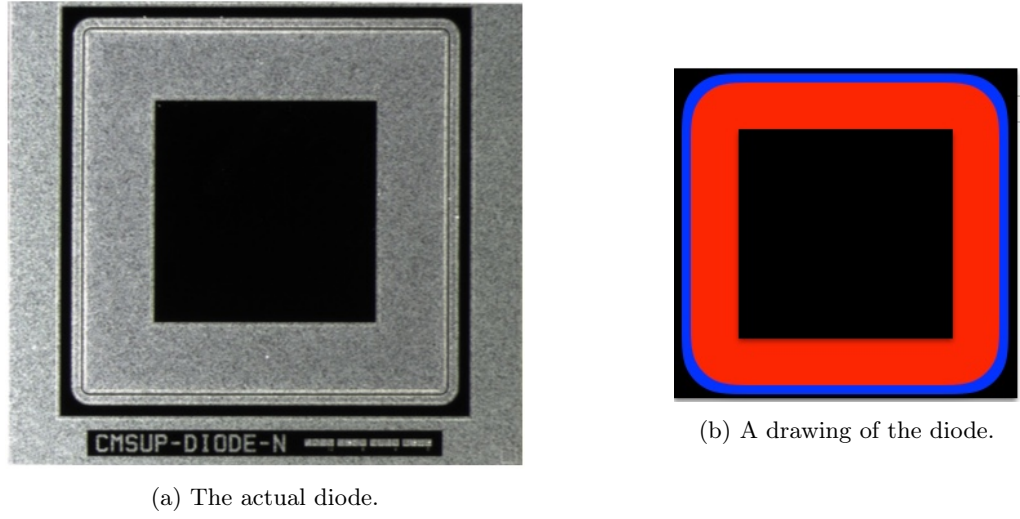


Figure 3.1.1: Large diode test structure.

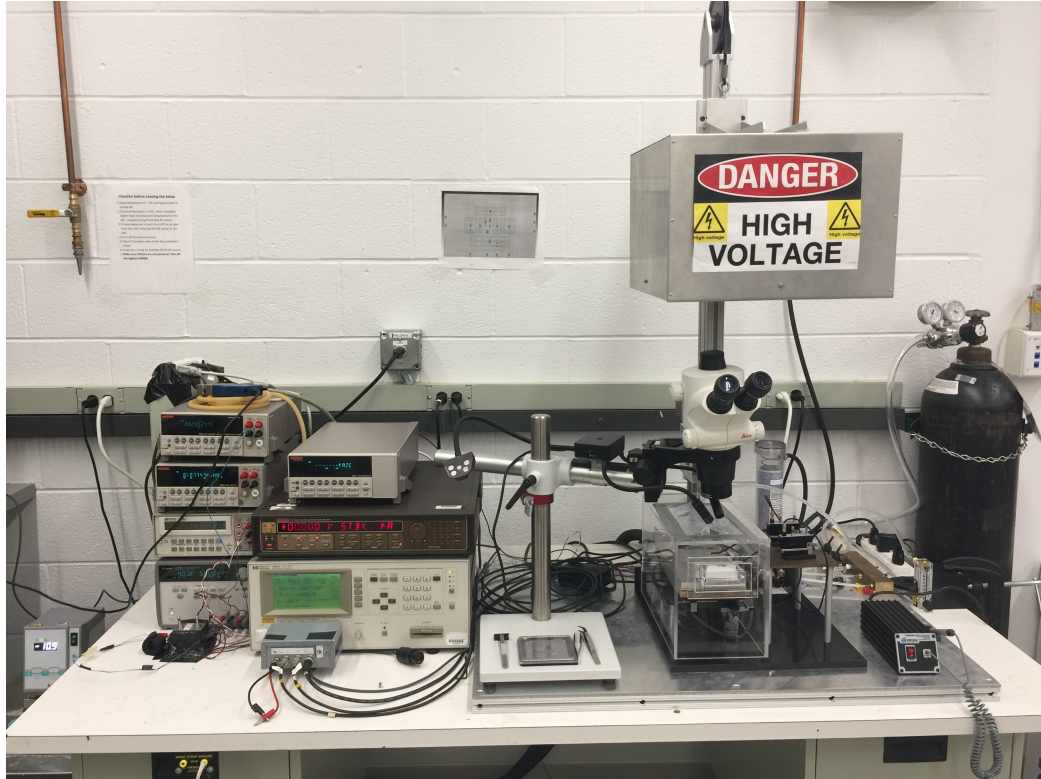


Figure 3.2.1: A picture of the electrical characterization setup in the Brown Silicon Lab.

high voltage to the chuck with a Keithley 237 High Voltage Measure Unit (± 1000 V). This same instrument then measures the current in the bias ring using probes (represented in Figure 3.2.2 by the black arrows) with a tip size of $7 \mu\text{m}$. All of the devices are controlled by LabView through a GPIB connection. For each voltage, the current is an average of four individual measurements with

a delay of 0.5 sec per measurement. Care is taken to note any anomalous behavior and, if present, the entire measurement is repeated to ensure that said behavior is a characteristic of the diode and not the equipment. For each annealing step, CVIV measurements are performed on each diode at both 0°C and -20°C.

The following procedures for both the IV and CV measurements describe the process that was used on all diodes measured in 2017 by myself and Soumya Ghosh. Analyses were also performed on data taken in 2016 by an undergraduate research assistant. Thus, the procedure followed for those measurements may not be exactly the same as the procedure described here. This difference will be discussed further in Chapter 5.

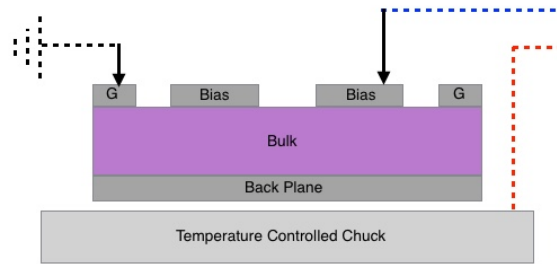


Figure 3.2.2: A drawing of the electrical characterization setup.

3.2.1 Current-Voltage Measurement (IV)

When performing a current-voltage measurement (IV), the blue and red dotted lines in Figure 3.2.2 go to the input and output of the Keithley 237, respectively. For the large diodes, the guard ring current is measured using a Keithley 6485 Picoammeter. For the small diodes, only the bias ring current is measured using the Keithley 237 because the small diodes do not have a guard ring.

3.2.2 Capacitance-Voltage Measurement (CV)

When performing a capacitance-voltage measurement (CV), both the blue and red dotted lines in Figure 3.2.2 go to an isolation box, which contains two capacitors connected to an HP 4284A LCR Meter. The capacitors in the isolation box prevent the LCR meter from receiving fatal voltages and currents. The LCR meter outputs a small AC voltage into the circuit containing the diode at two separate frequencies. The reaction of the circuit is then measured to determine the capacitance of the diode. Two different frequencies are used to ensure there are no resonance effects. For a more detailed discussion, see [1].

3.2.3 Variable Control

As with any experiment, there are many subtleties in measurement procedure that occur during data acquisition. In this section those subtleties will be discussed.

3.2.3.1 Temperature Control

As one can imagine, variations in the environment can greatly effect the accuracy of the measurements. Indeed, it was discovered that variations in temperature greater than $\pm 0.05^{\circ}\text{C}$ from the desired chuck temperature caused anomalous behavior in the data that was not present when the measurement was repeated. For the duration of data acquisition of all diodes measured in 2017, the temperature variations were kept within $\pm 0.04^{\circ}\text{C}$. However, it is not known whether this was followed for measurements taken in 2016.

3.2.3.2 Dew Point Control

In order to ensure that no condensation formed on the diodes during measurement, the dew point inside the acrylic box was constantly monitored. The temperature of the diode was assumed to be at the same temperature of the chuck, since the diode is extremely small and thin relative to the size of the chuck and the two are in thermal contact. If the dew point temperature inside the acrylic box came within $\pm 2^{\circ}\text{C}$ of the chuck temperature, the temperature of the chuck was raised accordingly via LabView control. Thus, in order for the temperature of the chuck to have the “small” variation ($\pm 0.04^{\circ}\text{C}$) mentioned above, the dew point is kept at least 5°C lower than the desired chuck temperature to avoid the aforementioned safety margin of 2°C from being crossed.

3.2.3.3 Humidity Control

Another method used to control the environment was the introduction of dry air into the acrylic box to keep the humidity $< 20\%$, as well as, an industrial humidifier in the lab itself. The dry air was flushed through a DRIERITE desiccant to further remove moisture. Controlling the humidity also helps to lower the dew point temperature. When performing measurements at -20°C , nitrogen was used instead of dry air, as this allowed the dew point to remain below -25°C . In many cases, the humidity was able to be kept below 10%.

Chapter 4

Analysis

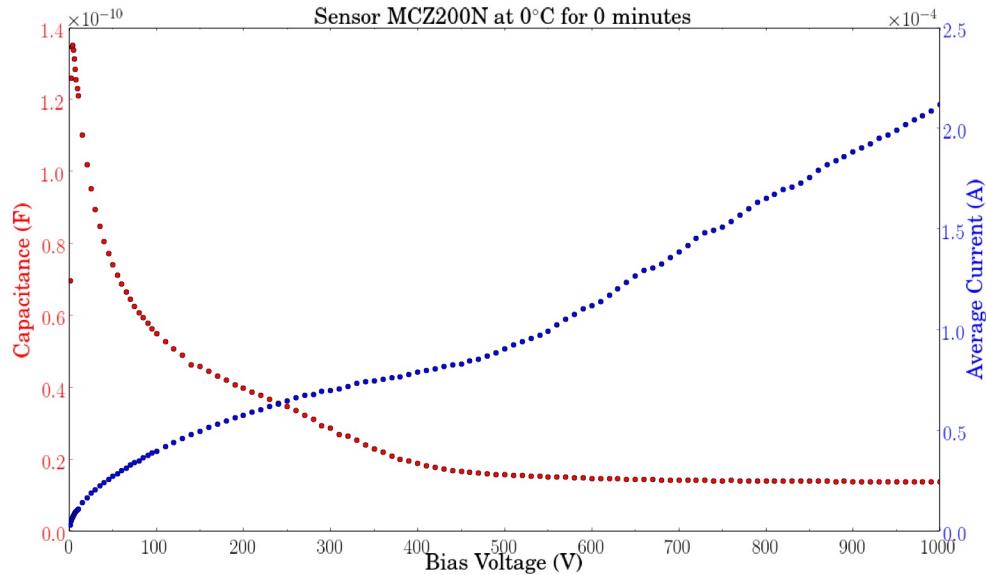


Figure 4.0.1: A typical CVIV plot of voltage versus capacitance. This particular plot is of the diode MCZ200N.

The analysis on the CVIV data is used to track the current related damage rate, α , and the change in the effective doping concentration, ΔN_{eff} , for increasing annealing times. To do this, the leakage current, related to α by Equation 2.2.1, and the depletion voltage, related to ΔN_{eff} by Equation 2.2.3, is extracted from the data.

4.1 Parameter Extraction

A typical CVIV plot is shown in Figure 4.0.1 and its behavior can be understood by examining Equations 2.2.5 and 2.2.6.

At zero volts, the depletion zone is at it's smallest width. Recall, that with a reverse biased diode an increase in applied voltage results in an increase in the width of the depletion zone. Thus, as the applied voltage increases so does the width of the depletion zone until the diode has been fully depleted and the width of the depletion zone is the same as the width of the bulk of the diode. Since the width of the depletion zone is proportional to $1/C$, the capacitance is highest at zero volts and continues to decrease until the diode is fully depleted, where it reaches an approximately constant value, the geometric capacitance, C_{geo} .

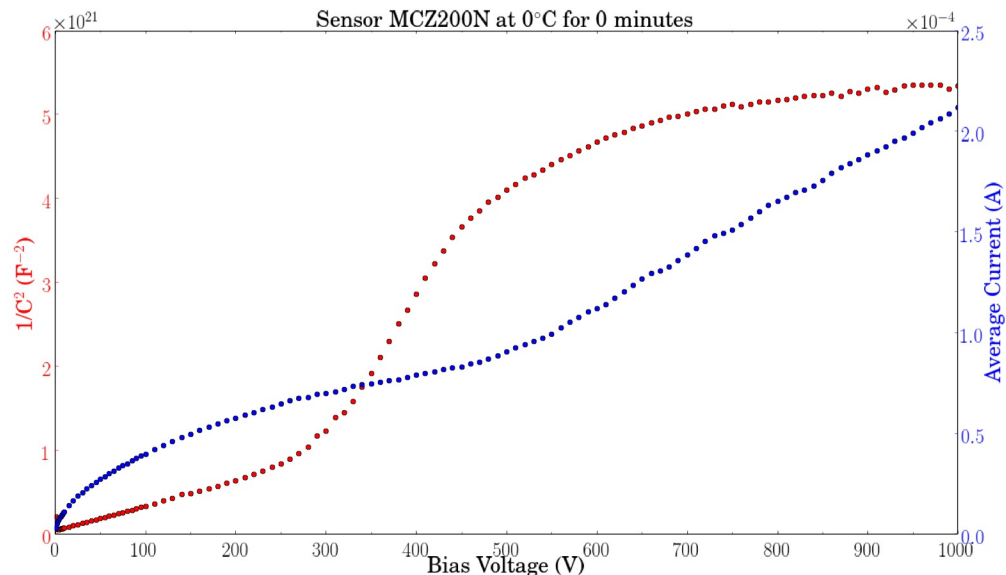


Figure 4.1.1: A typical plot of $1/C^2$ versus voltage. This particular plot is of the diode MCZ200N.

In order to extract the parameters, $1/C^2$ versus applied voltage is plotted for each diode at each annealing step at both temperatures, 0°C and -20°C . A typical plot is shown in Figure 4.1.1. The graph can be understood by rewriting Equation 2.2.5 as,

$$\frac{1}{C(V)^2} = \frac{2}{A^2 q_0 \epsilon_s \epsilon_0 |N_{\text{eff}}|} V, \quad (4.1.1)$$

where V_{bi} has been excluded because it is negligible. By examining Equation 4.1.1, we would expect Figure 4.1.1 to be a straight line, which is, in fact, what would be seen in a normal diode. However,

recall that these diodes have been irradiated and thus their properties have changed. Referring to Figure 4.1.1, there appear to be three “sections” where there is linear behavior: from 0 V to \sim 250 V, from \sim 300 V to \sim 450 V, and from \sim 700 V to 1000 V. The last one is the section where full depletion has been reached and the capacitance is approximately constant with a value of C_{geo} . The second section, from \sim 300 V to \sim 450 V, is where the diode is approaching full depletion. Therefore, the depletion happens somewhere between \sim 450 V and \sim 700V. To determine the depletion voltage, the second section and the last section are both fitted with a line; where the two lines intersect is the depletion voltage and the value of the current at that voltage is the leakage current at full depletion. Figure 4.1.2 shows this process being performed where the magenta line is where the two fit lines intersect.

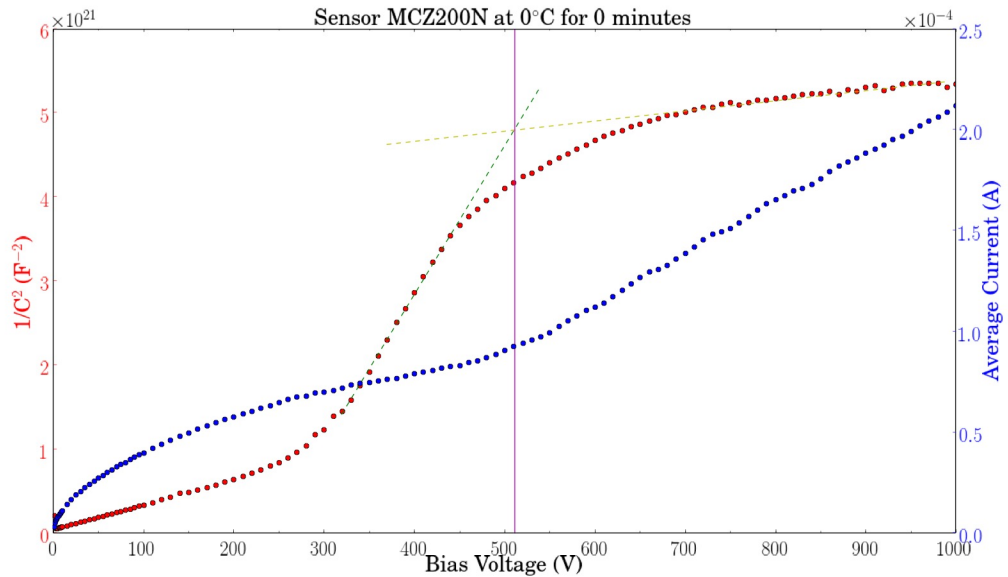


Figure 4.1.2: A plot of the extraction procedure for diode MCZ200N.

4.2 Results

The following describe the results of measurements and analyses. Those measurements with a maximum annealing time of eighty minutes were performed in 2016 by an undergraduate research assistant, while those measurements with a maximum annealing time of forty minutes were performed in 2017 by myself or Soumya Ghosh.

4.2.1 Current Related Damage Rate

The overall change in the current related damage rate, α , are shown in Figures 5.3.1 through 5.3.3. The changes seen at -20°C are broken up into two figures only because the range of α was too large to show detailed behavior with all measurements on one plot. Plots showing multiple lines with the same color contain measurements with the guard ring both connected and disconnected.

4.2.2 Effective Doping Concentration

The overall change in the effective doping concentration, N_{eff} , are shown in Figures 5.3.4 through 5.3.6. Again, some plots are broken up into two figures and plots showing multiple lines with the same color contain measurements with the guard ring both connected and disconnected.

4.2.3 Error Propagation

The errors presented in the plots of the results were calculated based on the errors in the slopes of the performed fits. The propagation was found using the following formula,

$$\delta F = \sqrt{\sum_i \left(\frac{\partial F}{\partial x_i} \right)^2 (\delta x_i)^2} \quad (4.2.1)$$

where x_i is the i th variable and δx_i is the uncertainty in the i th variable. Possible improvements in measurement procedure will be discussed in Chapter 5.

Chapter 5

Conclusions

Referring to Figures 2.3.2 and 2.3.1, the expected behavior, found in [1] and [6], is that both parameters decrease over the annealing times studied. Recall that for effective doping concentration, after short-term annealing comes an increase in N_{eff} during the “reverse annealing” period. However, this occurs at annealing times greater than those studied.

5.1 Current Related Damage Rate

All diodes studied showed a decrease in the current related damage rate and thus, behaved as expected. A fit with Equation 2.3.1 was attempted, but no correlation was found. In order to verify the expected further decrease of α with increasing annealing time, this study should be continued by further annealing and CVIV measurement.

5.2 Effective Doping Concentration

All diodes studied, except for FTH200N at -20°C, showed a decrease in the effective doping concentration and thus, behaved as expected. The exact reason for the anomalous behavior of FTH200N cannot be known as this data was taken in 2016, as mentioned in Section 4.2. In order to verify the expected behavior, decrease followed by increase and possible type inversion, of N_{eff} with increasing annealing time, this study should be continued by further annealing and CVIV measurement.

5.3 The Future

As was stated in Chapter 1, it is of the utmost importance that these studies continue for the tracker to survive the full length of the experiment after the CMS upgrade. The difficulty comes in the study of highly irradiated and multiply annealed sensors, which become highly erratic over time. For those measurements taken in 2017, the most important factors seemed to be controlling the temperature variation on the chuck ($\pm 0.04^\circ\text{C}$) and ensuring a good connection with the probes.

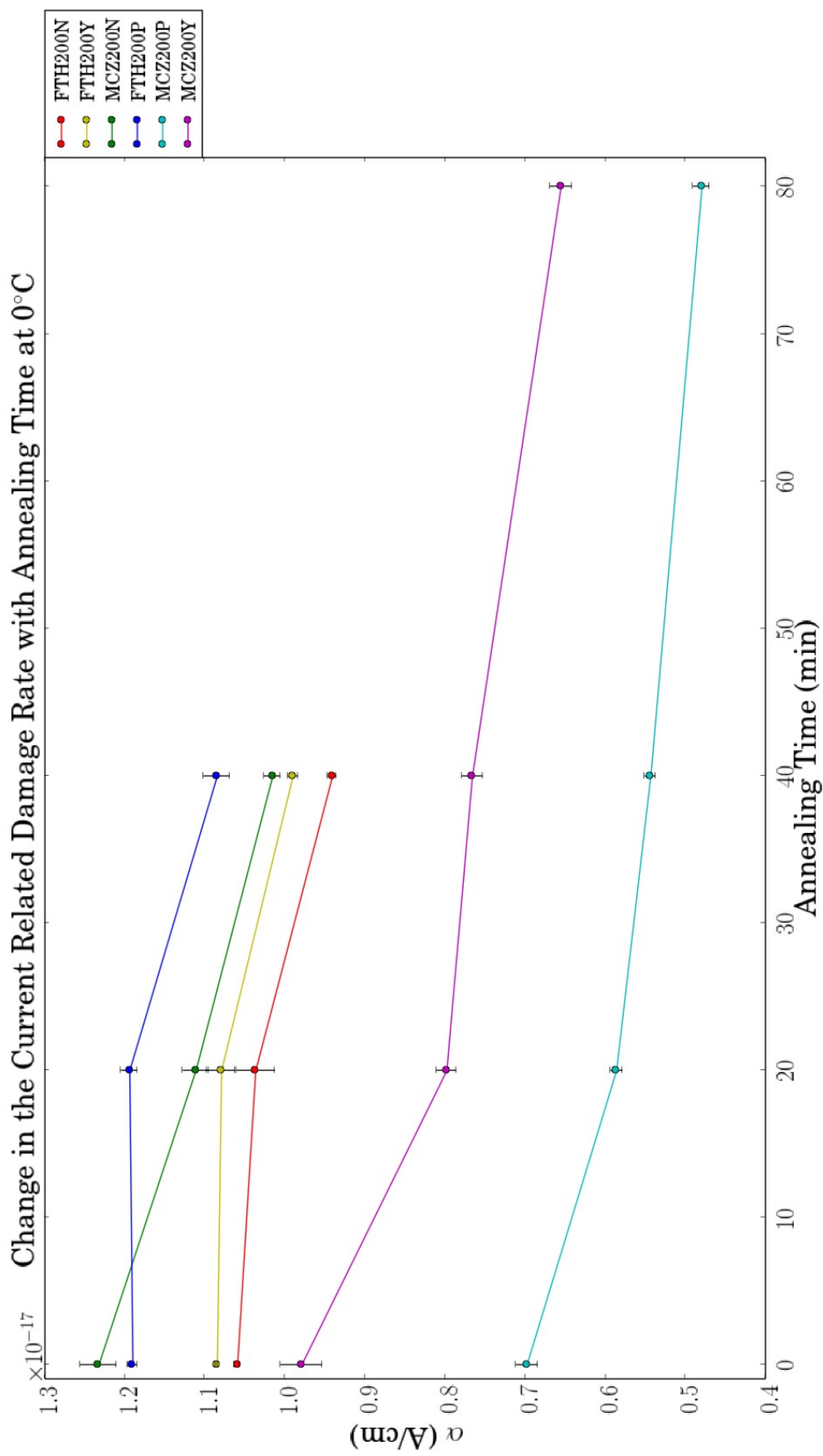


Figure 5.3.1: The change in the current related damage rate at 0°C.

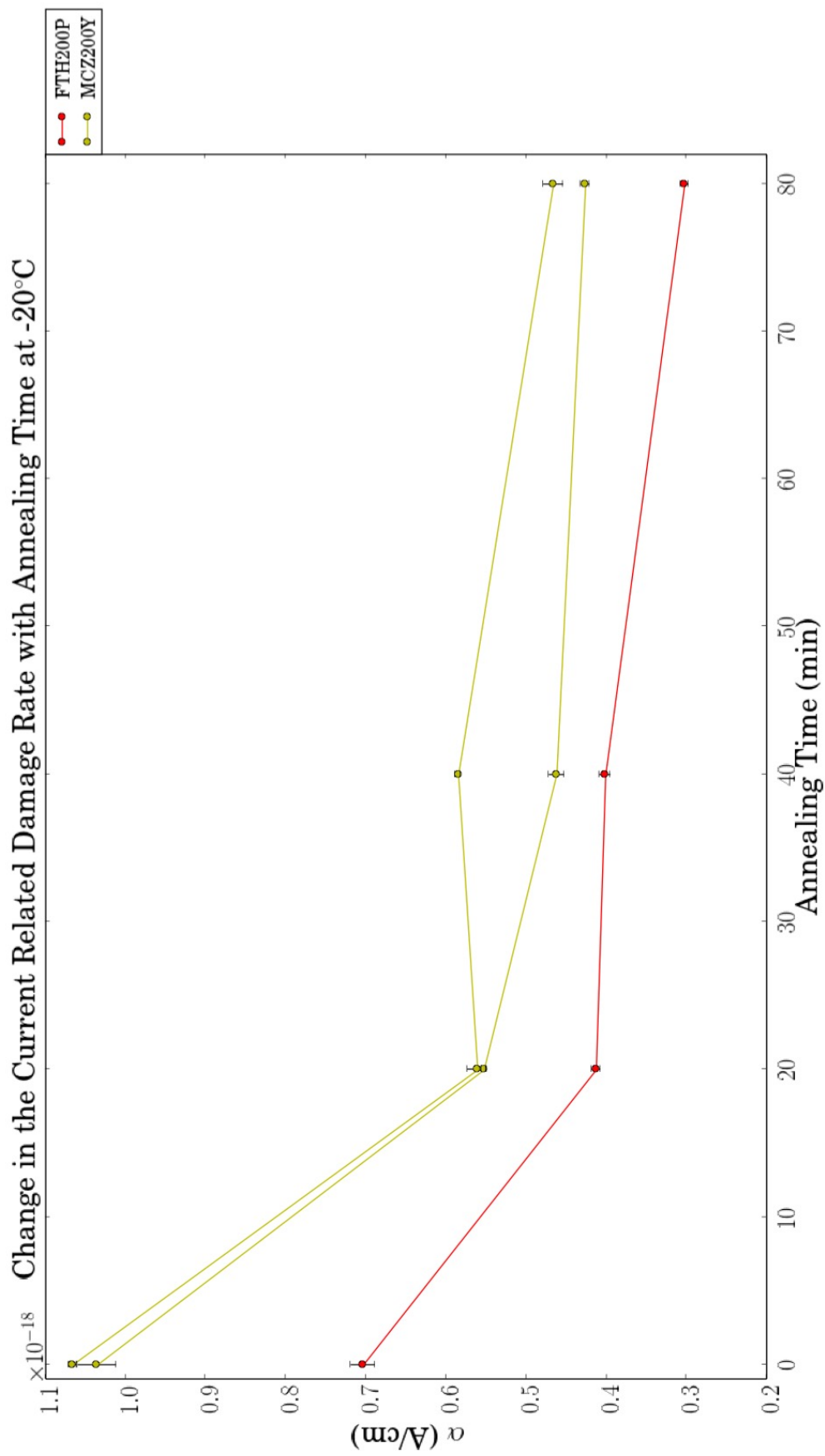


Figure 5.3.2: The change in the current related damage rate at $-20^\circ C$.

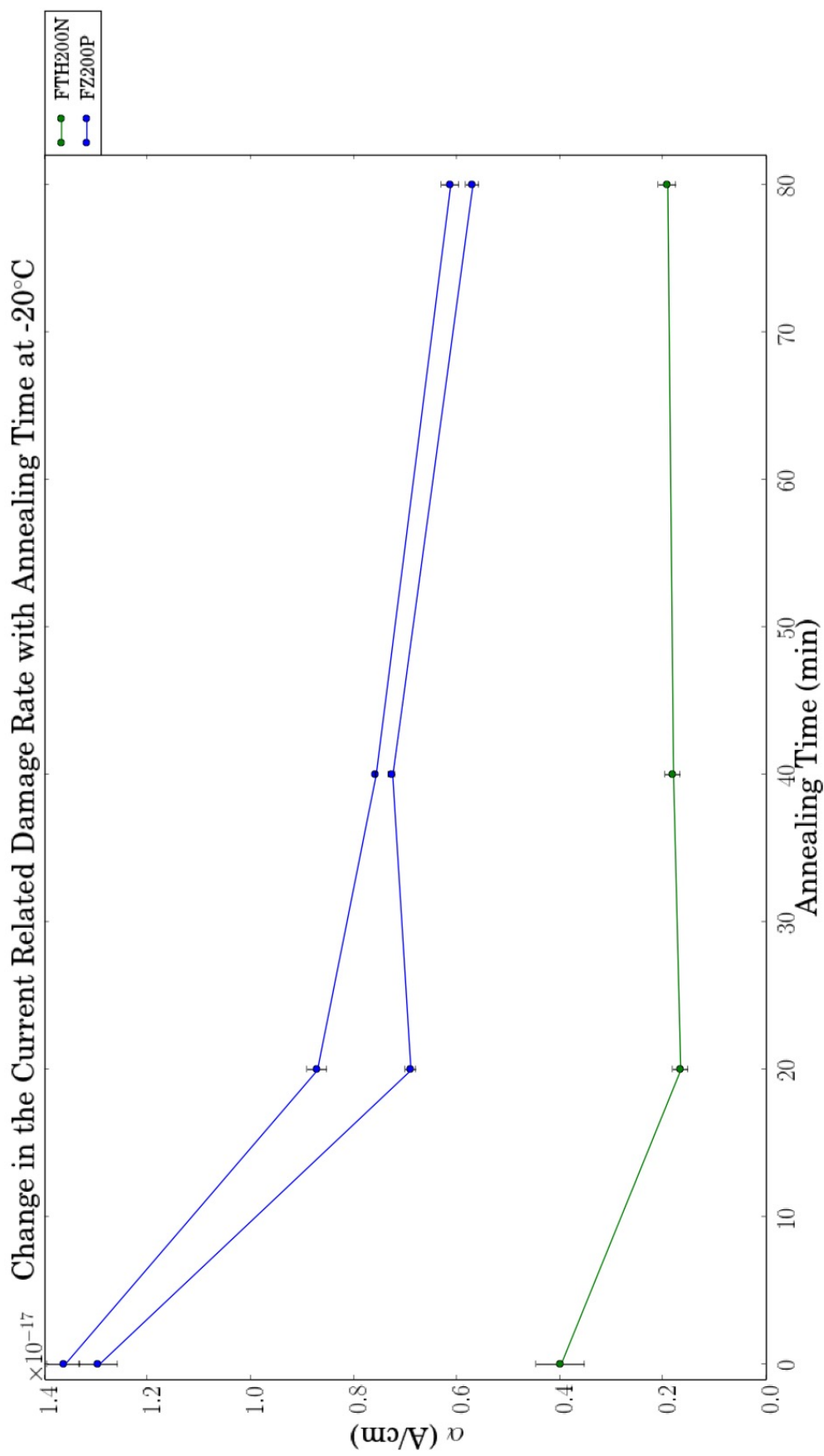


Figure 5.3.3: The change in the current related damage rate at -20°C .

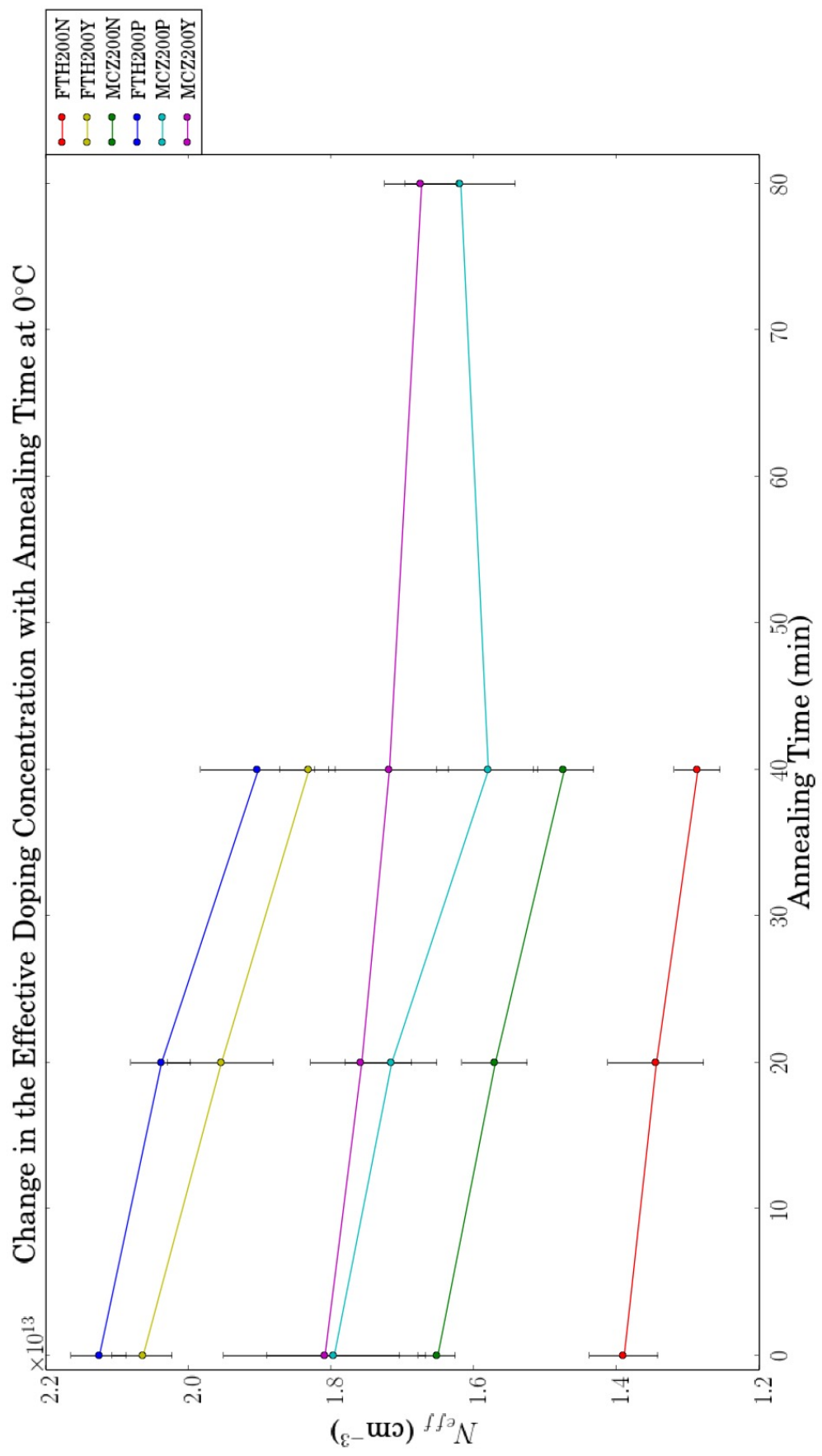


Figure 5.3.4: The change in the effective doping concentration at 0°C.

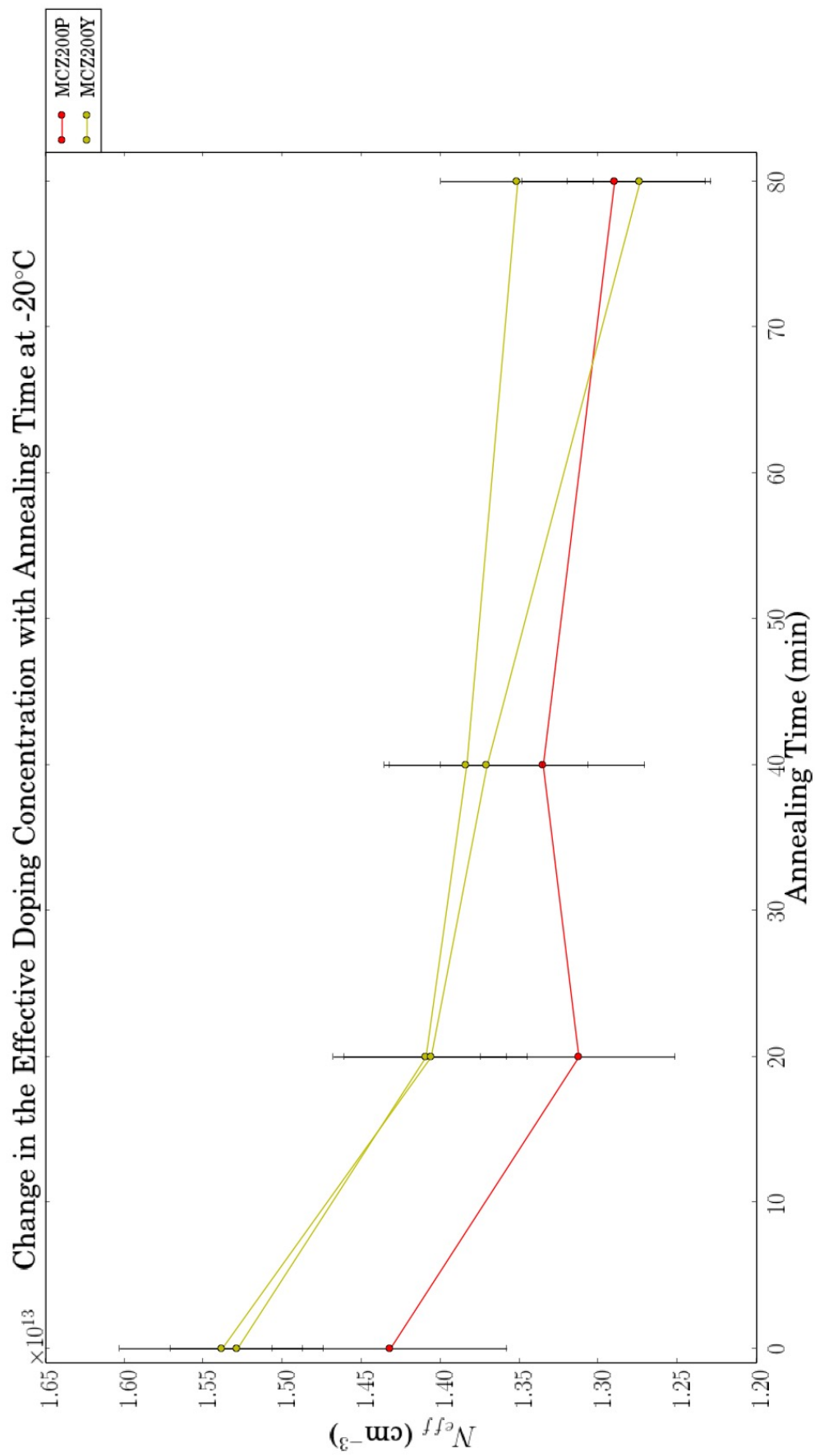


Figure 5.3.5: The change in the effective doping concentration at -20°C .

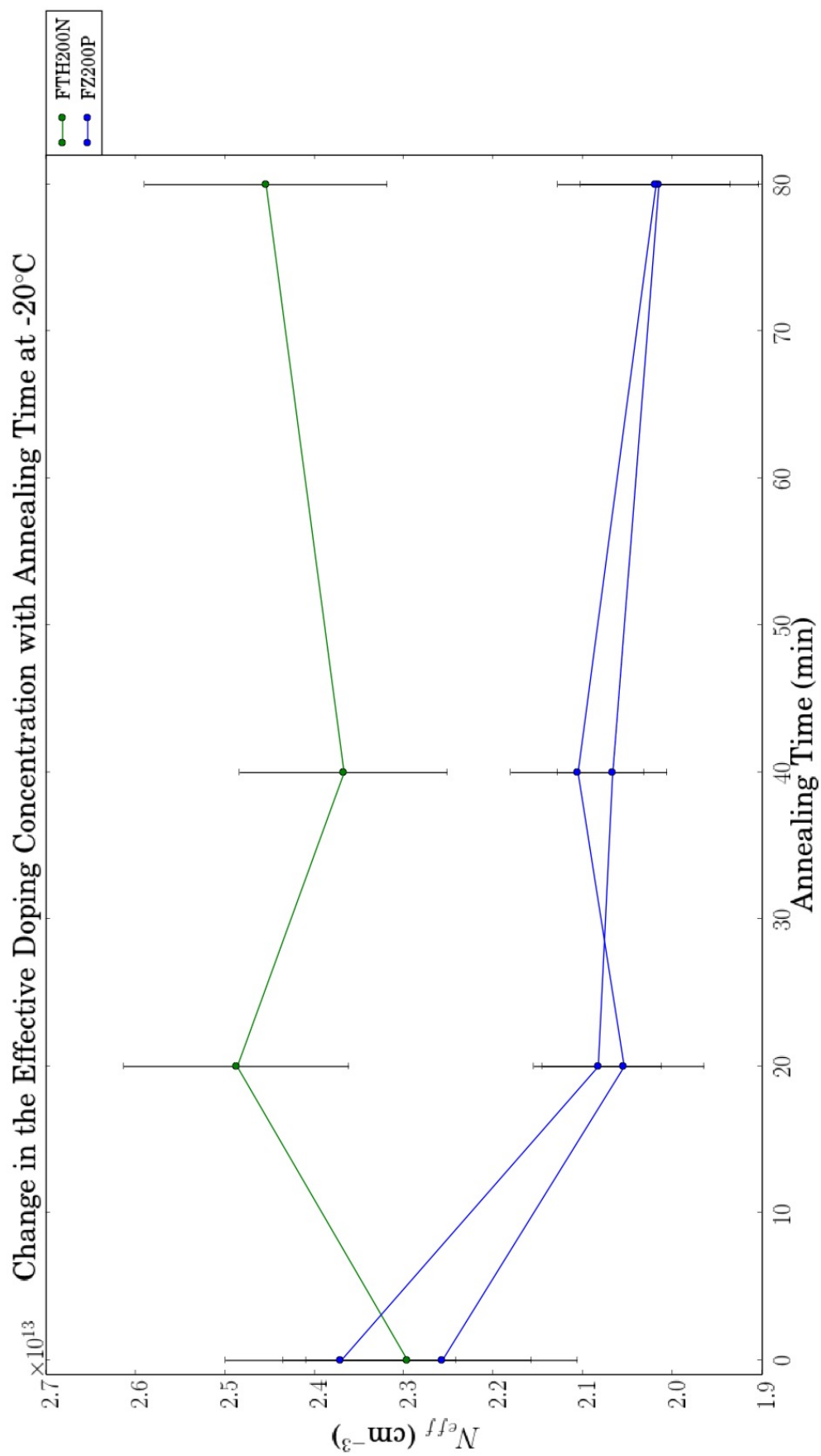


Figure 5.3.6: The change in the effective doping concentration at -20°C .

Bibliography

- [1] M. Moll, "Radiation Damage in Silicon Particle Detectors". PhD thesis, University of Hamburg, 1999.
- [2] D. Contardo (ed.), M. Klute (ed.), J. Mans (ed.), L. Silvestris (ed.), J. Butler (ed.). "Technical Proposal for the Phase-II Upgrade of the CMS Detector". Report Number: CERN-LHCC-2015-010 ; LHCC-P-008 ; CMS-TDR-15-02. June 2015.
- [3] M. Printz, "Radiation hard sensor materials for the DMS Tracker Phase II Upgrade - Charge collection of different bulk polarities". Nuclear Instruments and Methods in Physics Research A 765 (2014) 29-34. April 2014.
- [4] J. Pulko, "Radiation Damage in Silicon Detectors". Seminar. April 2007.
- [5] D. Horak, "Measurement of Silicon Particle Detector Properties". Bachelor Thesis, Czech Technical University in Prague, 2013.
- [6] S. Sagir, "Search for Heavy Top Quark Partners with Charge 5/3 and Anomalous Higgs ($\rightarrow b\bar{b}$) Couplings to Vector Bosons". PhD thesis, Brown University, 2017.
- [7] G. Casse, "The Effect of Hadron Irradiation on the Electrical Properties of Particle Detectors Made from Various Silicon Materials". PhD thesis, Joseph Fourier University, 1998.
- [8] R. Eber, "Investigations of new Sensor Designs and Development of an effective Radiation Damage Model for the Simulation of highly irradiated Silicon Particle Detectors". PhD thesis, Karlsruhe Institute of Technology, 2013.
- [9] L. Rossi, P. Fischer, T. Rohe, N. Wermes. "Pixel Detectors: From Fundamentals to Applications". New York: Springer, 2005.